Simulation of long-term rotational dynamics of large space debris: A TOPEX/Poseidon case study

Luc B.M. Sagnières [a,b,*], Inna Sharf [a], Florent Deleflie [b]

[a] *McGill University, Department of Mechanical Engineering, 817 Sherbrooke Street West, Montreal, Quebec H3A 0C3, Canada*
[b] *IMCCE, Observatoire de Paris, PSL Research University, CNRS, Sorbonne Université, Université de Lille, 77 Avenue Denfert Rochereau, 75014 Paris, France*

Abstract

Accurate knowledge of the rotational dynamics of a large space debris is crucial for space situational awareness (SSA), whether it be for accurate orbital predictions needed for satellite conjunction analyses or for the success of an eventual active debris removal mission charged with stabilization, capture and removal of debris from orbit. In this light, the attitude dynamics of an inoperative satellite of great interest to the space debris community, the joint French and American spacecraft TOPEX/Poseidon, is explored. A comparison of simulation results with observations obtained from high-frequency satellite range measurements is made, showing that the spacecraft is currently spinning about its minor principal axis in a stable manner. Predictions of the evolution of its attitude motion to 2030 are presented, emphasizing the uncertainty on those estimates due to internal energy dissipation, which could cause a change of its spin state in the future. The effect of solar radiation pressure and the eddy-current torque are investigated in detail, and insights into some of the satellite's missing properties are provided. These results are obtained using a novel, open-source, coupled orbit-attitude propagation software, the Debris SPin/Orbit Simulation Environment (D-SPOSE), whose primary goal is the study of the long-term evolution of the attitude dynamics of large space debris.
© 2019 COSPAR. Published by Elsevier Ltd. All rights reserved.

Keywords: Space debris; Attitude dynamics; Satellite laser ranging; TOPEX/Poseidon; D-SPOSE

1. Introduction

The space debris population around Earth has been steadily increasing since the beginning of the Space Age. Mitigation efforts have increased in the last two decades and while stopping the trend is crucial for the safety of future space operations, coming back to a stable space environment can only be achieved by removing current debris from orbit (Liou and Johnson, 2006). As such, reme-diation efforts, including Active Debris Removal (ADR) missions, are being developed around the world. These missions consist of the launch of a removal spacecraft which would rendezvous with a large debris target, capture and stabilize it, and finally remove it from orbit, either by burning it in the atmosphere, or by placing it in a disposal orbit (Shan et al., 2016). These efforts, however, can only succeed if an accurate estimation of the target's rotational state is obtained prior to launch. Knowing the target's spin parameters is critical for the stabilization and capture stage. In this light, multiple observation campaigns of high-value targets in densely populated orbits are underway (Kucharski et al., 2017, 2014; Koshkin et al., 2016; Earl and Wade, 2015), and, in parallel, modelling efforts are trying to characterize the long-term evolution of the attitude

dynamics of defunct satellites. In combination, these efforts will improve the understanding and forecasting of the dynamics of these possible targets (Efimov et al., 2018,; Kanzler et al., 2015; Albuja et al., 2018). The goal of this work is to contribute to the understanding of the attitude dynamics of defunct spacecraft by investigating the rotational motion of the decommissioned joint NASA/CNES Ocean Topography Experiment called TOPEX/Poseidon.

TOPEX/Poseidon was initially launched in August 1992 into a circular orbit at 1,340 km with a 66° inclination, with a purpose to precisely map ocean surface topography in order to study various global weather phenomena (Fu et al., 1994). It was decommissioned in 2006 after one of its momentum wheels stopped working, and since then has seen an increase in its angular velocity, as observed by SLR (Satellite Laser Ranging) and light curves; this spin-up has been attributed to solar radiation pressure (Kucharski et al., 2017; Kudak et al., 2017). As the satellite contains a retroreflector array, precise measurements of its spin period and spin axis orientation have been obtained through high-repetition rate SLR data since 2014 from the Graz SLR station in Austria (Kucharski et al., 2017). The International Laser Ranging Service (ILRS) and its Space Debris Working Group then initiated a global observation campaign in 2015.

The interest in this debris has recently been even more pressing after a very close approach of 400 m was noticed in June 2017 between TOPEX/Poseidon and one of its successor spacecraft, the NASA/CNES Jason-2 satellite (Kucharski et al., 2017). On top of understanding its rotational motion, knowing its attitude dynamics is also beneficial to obtain precise orbital predictions for conjunction analyses: to determine whether orbital manoeuvres of active satellites are necessary. However, accurate estimates of the spacecraft properties needed to predict the evolution of its rotation are absent in the literature. Unlike for other satellites, there are no inertia parameter estimates available for TOPEX/Poseidon, and its magnetic properties and solar panel orientation are unknown. The following study will aim to shed light on some of these missing parameters by comparing simulation results to precise SLR measurements obtained for TOPEX/Poseidon. This case study will provide a better understanding of the underlying rotational dynamics of this defunct satellite. The unknown spacecraft parameters will be investigated, and future estimates of the satellite's attitude state will be put forward.

The investigation of TOPEX/Poseidon's missing parameters and its rotation motion evolution is carried out using a novel coupled orbit-attitude propagator called D-SPOSE (Debris SPin/Orbit Simulation Environment), which builds on the dynamics model previously applied to the defunct European satellite Envisat (Sagnières and Sharf, 2019) and which is available as an open-source software.[1] Its primary purpose is to function as a highly adaptable and comprehensive software for large defunct satellites (>10 cm) in order to study their attitude dynamics and derive a concrete understanding of their long-term evolution (order of years).

The model behind D-SPOSE will first be introduced in Section 2. Section 3 will introduce the past observations of TOPEX/Poseidon's spin motion determined from SLR measurements and the associated findings. Section 4 will then provide a comprehensive analysis of the rotational dynamics of TOPEX/Poseidon, comparing simulations results with observational data and investigating the effect of individual perturbations. Finally, a discussion and summary of findings will be outlined in Section 5 and a conclusion will be presented in Section 6.

2. Debris SPin/Orbit simulation environment

2.1. Spacecraft dynamics

Dealing with satellite dynamics requires an analysis of the six degrees of freedom governing the orbit and attitude of spacecraft. Three coupled vector differential equations describe the evolution of the corresponding variables (Sagnières and Sharf, 2019): first is the dynamics equation for orbital motion in an Earth-Centered Inertial (ECI) coordinate frame (Vallado, 2013, Ch. 8, p. 525); second is the dynamics equation for attitude motion (Hughes, 2006, Ch. 3 p. 59); and third the kinematic equation for the absolute orientation of the spacecraft.

In D-SPOSE, the aforementioned equations are numerically propagated at a fixed integration time step using a fifth-order Runge-Kutta method called the Runge-Kutta Dormand-Prince (RKDP) numerical integration method (Dormand and Prince, 1980). The same time step is used for propagating both the orbit and attitude equations as they are coupled, where information about one is used in the computation and propagation of the other.

The chosen ECI frame used to propagate these equations is the True Equator Mean Equinox (TEME) reference frame. The TEME frame is not truly inertial, however, and slowly rotates with time as the true equator shifts. Nevertheless, it was determined that currently a rate of change of approximately 0.005° per year occurs with respect to the J2000 ECI frame. This was deemed negligible for studies of large space debris as the usual propagation time scale is on the order of a decade.

The accelerations and torques due to external perturbations as well as the environmental models considered for TOPEX/Poseidon are summarized in Table 1. These include Earth's gravitational acceleration due to its deviation from that of a homogeneous sphere, the gravity-gradient torque, and third-body gravitational accelerations from the Sun and the Moon as point masses, all of which are conservative, as well as the eddy-current torque and the radiation pressure and torque, which are non-conservative. Direct solar radiation as well as reflected radiation (albedo) and infrared emission from the Earth are considered. The effect of internal energy dissipation is

---

Table 1
External perturbations and environmental models employed for TOPEX/Poseidon.

Perturbation	Environmental Model
Gravitational perturbations and Gravity gradient torque	EGM2008
Third-body perturbations	Miriade Ephemerides
Eddy-current torque	IGRF-12
Solar radiation pressure and torque	Montenbruck and Gill
Albedo acceleration and torque	Stephens
Infrared acceleration and torque	Stephens
Internal energy dissipation	Kane Damper

also taken into account. As TOPEX/Poseidon is in a relatively high orbit (1340 km), the effects of aerodynamic drag and torque are neglected in this study. The relevant perturbations and the associated environmental models will be discussed in detail in Sections 2.2 and 2.3.

2.2. Gravitational perturbations

The gravitational acceleration, $\mathbf{a}_{\mathrm{grav}}$, is obtained from a spherical-harmonic expansion of the Earth's gravitational potential function, U, defined in the Earth-Centered Earth-Fixed (ECEF). It is computed as a function of its geocentric distance, r, its spherical geocentric latitude, θ, and its longitude, λ, and is derived using the chain rule (Vallado, 2013, Ch. 8, p. 550):

$$\mathbf{a}_{\mathrm{grav}} = \frac{\partial U}{\partial r}\left(\frac{\partial r}{\partial \mathbf{r}}\right)^T + \frac{\partial U}{\partial \lambda}\left(\frac{\partial \lambda}{\partial \mathbf{r}}\right)^T + \frac{\partial U}{\partial \theta}\left(\frac{\partial \theta}{\partial \mathbf{r}}\right)^T \quad (1)$$

The gravitational model available in D-SPOSE is the Earth Gravitational Model 2008 (EGM2008) (Pavlis et al., 2012).

The non-uniform distribution of the gravitational field over the spacecraft body leads to a gravity-gradient torque. It is a conservative torque and will therefore not have a long-term effect on the rotational energy of a spacecraft but will have an influence on the evolution of its spin axis. The gravity-gradient torque is usually calculated assuming a spherical model of Earth's gravity field. In D-SPOSE, in order to provide a more accurate analysis of the effect of the Earth's gravitational field on the long-term attitude dynamics of large space debris, it is computed for a general gravitational field from the spherical-harmonic expansion of the geopotential. The gravity-gradient torque is then given as follows (Gottlieb, 1993):

$$\tau_{\mathrm{grav}} = \begin{bmatrix} g_{23}(I_{zz} - I_{yy}) - g_{13}I_{xy} + g_{12}I_{xz} + I_{yz}(g_{22} - g_{33}) \\ g_{13}(I_{xx} - I_{zz}) + g_{23}I_{xy} - g_{12}I_{yz} + I_{xz}(g_{33} - g_{11}) \\ g_{12}(I_{yy} - I_{xx}) - g_{23}I_{xz} + g_{13}I_{yz} + I_{xy}(g_{11} - g_{22}) \end{bmatrix} \quad (2)$$

where the g_{ij} and I_{ij} are the components of the matrices $\mathbf{G}$ and $\mathbf{I}$, respectively, the former defined by (Gottlieb, 1993):

$$\mathbf{G} = \mathbf{C}^T \frac{\partial \mathbf{a}_{\mathrm{grav}}}{\partial \mathbf{r}} \mathbf{C} \quad (3)$$

and where $\mathbf{C}$ is the rotation matrix from the body-fixed frame to the inertial frame.

The derivative of $\mathbf{a}_{\mathrm{grav}}$ with respect to $\mathbf{r}$, required to evaluate $\mathbf{G}$, can be computed from Eq. (1) by again applying the chain rule, with the second partial derivatives and additional coordinate transformations derived in closed form, as presented in Sagnières and Sharf (2019).

The final gravitational perturbations considered are third-body accelerations due to the Moon and the Sun. Their effect is determined from μ_k and $\mathbf{r}_k$ representing the gravitational parameter and position of the Sun and Moon ($k = 1, 2$) in the chosen ECI frame, respectively, and treating them as point masses (Vallado, 2013, Ch. 8, p. 574):

$$\mathbf{a}_k = \sum_{k=1,2} \mu_k \left(\frac{\mathbf{r}_k(t) - \mathbf{r}(t)}{\|\mathbf{r}_k(t) - \mathbf{r}(t)\|^3} - \frac{\mathbf{r}_k(t)}{r_k(t)^3} \right) \quad (4)$$

The positions of the Sun and the Moon ($\mathbf{r}_1$ and $\mathbf{r}_2$) are obtained from planetary ephemerides provided by the Virtual Observatory of the Institut de Mécanique Céleste et de Calcul des Éphémérides (IMCCE, 2018).

2.3. Non-gravitational perturbations

2.3.1. Eddy-current torque

The interaction between a spinning satellite's conductive surfaces and the Earth's magnetic field will lead to a perturbing eddy-current torque. This phenomenon arises from the rotation of an electrically conducting body as moving electrons are resisted by the surface material. For slowly spinning spacecraft, the time variation of the magnetic field as seen by the orbiting spacecraft also needs to be considered, an effect rarely considered in the literature and which was not included in the dynamics model described in our previous work (Sagnières and Sharf, 2019). The equation for the eddy-current torque, in body frame components, is (Efimov et al., 2018):

$$\tau_{\mathrm{eddy}} = \left[\mathbf{M}\left(\omega^{\times} \mathbf{B} - \frac{d\mathbf{B}}{dt} \right) \right]^{\times} \mathbf{B} \quad (5)$$

where $\mathbf{M}$ is the matrix representation of the magnetic tensor of the object (Ortiz Gómez and Walker, 2015), $\mathbf{B}$ is the Earth's magnetic field, and $\frac{d\mathbf{B}}{dt}$ is the aforementioned time derivative of the Earth's magnetic field measured in the inertial frame, as experienced along the satellite's orbit and expressed in the body-fixed frame. The Earth's magnetic field can be calculated similarly to the effect of the Earth's gravity field from the spherical-harmonic expansion of the Earth's magnetic potential in the ECEF frame.

The time derivative of the Earth's magnetic field can be calculated from the magnetic field in a rotating ECEF frame using:

$$\frac{d\mathbf{B}}{dt} = \left(\frac{d\mathbf{B}}{dt}\right)_E + \omega_E^{\times} \mathbf{B} \quad (6)$$

where ω_E is the angular velocity of the Earth with respect to the inertial frame. The time derivative of the magnetic

field measured in the ECEF frame can then be further expanded as:

$$\left(\frac{d\mathbf{B}}{dt}\right)_E = (\mathbf{v}_E \cdot \nabla)\mathbf{B} + \left(\frac{\partial \mathbf{B}}{\partial t}\right)_E \tag{7}$$

where $\mathbf{v}_E$ is the spacecraft velocity measured in the rotating ECEF frame, that is:

$$\mathbf{v}_E = \mathbf{v} - \boldsymbol{\omega}_E^\times \mathbf{r} \tag{8}$$

where $\mathbf{r}$ is the position of the satellite. Considering a local spherical coordinate frame, S (Sagnières et al., 2018):

$$\left(\frac{\partial \mathbf{B}}{\partial t}\right)_E = \left(\frac{\partial \mathbf{B}}{\partial t}\right)_S + \boldsymbol{\omega}_S^\times \mathbf{B} \tag{9}$$

where $\boldsymbol{\omega}_S$ is the angular velocity of the spherical coordinate frame with respect to the ECEF frame due to the orbiting spacecraft, defined by:

$$\boldsymbol{\omega}_S = \frac{\mathbf{r}^\times \mathbf{v}_E}{r^2} \tag{10}$$

Analytical expressions for Eqs. (6)–(10) obtained from the spherical-harmonic expression for the Earth's magnetic potential are stated in Sagnières et al. (2018). The geomagnetic potential model used to calculate the strength and direction of the magnetic field at the satellite position is the International Geomagnetic Reference Field (IGRF) (Thébault et al., 2015).

2.3.2. Radiation perturbations

The pressure that an incoming flux of photons has on satellite surfaces can lead to a non-negligible acceleration and torque, depending on the spacecraft shape. The force associated with radiation can be calculated as a double summation over every lit surface p and over every radiation source r and expressed as components in the inertial frame (Hughes, 2006, Ch. 8, p. 263):

$$\mathbf{a}_{\text{rad}} = \sum_p \sum_r \frac{\phi_r}{mc} \left[(\sigma_a + \sigma_{rd})\mathbf{s}_r + \frac{2}{3}\sigma_{rd}\mathbf{n}_p + 2\sigma_{rs}\cos\beta_r\mathbf{n}_p\right] A_p \cos\beta_r \tag{11}$$

where σ_a, σ_{rd}, and σ_{rs} represent the coefficients of absorption, diffuse reflection, and specular reflection for that surface and for the appropriate light spectrum, respectively, c is the speed of light, ϕ_r is the photon flux from the incoming source of radiation, $\mathbf{s}_r$ is the unit vector of the incident light direction, and $\cos\beta_r = \mathbf{s}_r \cdot \mathbf{n}_p$. Surfaces are considered to be in view of the radiation source when $\cos\beta_r > 0$.

The torque associated with the radiation can then be obtained from the acceleration derived above, summed over every lit surface p, and expressed in the body-fixed frame (Hughes, 2006, Ch. 8, p. 263):

$$\boldsymbol{\tau}_{\text{rad}} = \sum_p m\mathbf{c}_p^\times \mathbf{a}_{\text{rad},p} \tag{12}$$

Three sources of radiation leading to three photon fluxes are considered: first, and largest, direct solar radiation from the Sun, ϕ_{solar}; second, radiation reflected from the Earth's surface (albedo), ϕ_{alb}; and third, emitted infrared radiation from the Earth, ϕ_{ir}. The latter two are improvements with respect to our previous model described in Sagnières and Sharf (2019).

The solar radiation photon flux varies with time and can be calculated as (Kucharski et al., 2017):

$$\phi_{\text{solar}} = \psi_S S_R \left(\frac{a_u}{r_1}\right)^2 \tag{13}$$

where S_R is the solar radiation constant, a_u is the astronomical unit, and ψ_S is the Earth shadow function, which equals 0 when the satellite is in the Earth's shadow and 1 when the satellite is sunlit. A geometrical model of the penumbra transition when $0 < \psi_S < 1$ is used (Montenbruck and Gill, 2013, Ch. 3, p. 80).

The albedo and infrared radiation from the Earth have a smaller effect than direct solar radiation but still need to be taken into account. The effect of the albedo will be greatest when the satellite is on the dayside, where the Earth's surface below it is illuminated, while Earth's infrared emissions are independent of illumination. Photon fluxes also vary with time and location. By dividing Earth's surface into grids defined by latitude and longitude, one can calculate them as follows (Kucharski et al., 2017):

$$\phi_{\text{alb}} = S_R \left(\frac{a_u}{r_1}\right)^2 \sum_\theta \sum_\lambda \alpha_{\text{alb},\theta,\lambda} \cos\psi \cos\gamma \frac{A_{\theta,\lambda}}{\pi d} \tag{14}$$

$$\phi_{\text{ir}} = S_R \left(\frac{a_u}{r_1}\right)^2 \sum_\theta \sum_\lambda \alpha_{\text{ir},\theta,\lambda} \cos\gamma \frac{A_{\theta,\lambda}}{4\pi d} \tag{15}$$

where α_{alb} and α_{ir} are the albedo and emissivity coefficients, respectively, $A_{\theta,\lambda}$ is the Earth surface element area, d is the Earth surface element-satellite distance, and with ψ and γ representing the angles between the Earth surface element normal and the direction to the Sun and satellite, respectively. Earth surface elements are only considered when $\cos\gamma > 0$ for both albedo and infrared emissions, and also only when the surface element is lit, *i.e.*, when $\cos\psi > 0$, for the albedo. The incident light direction is calculated from the center of the considered Earth surface element.

The model for the Earth albedo and emissivity coefficients comes from a set of monthly-averaged values derived from satellite observations between 1964 and 1977 (Stephens et al., 1981). The data is divided into $9° \times 9°$ latitude-longitude bins with values for each the albedo and emissivity coefficients for every month of the year.

2.3.3. Internal energy dissipation

Internal energy dissipation is the last torque included as its effect is known to be significant in the long-term attitude motion of spacecraft. For TOPEX/Poseidon, it is specifically relevant as it will be shown that the spacecraft is spinning about its minor principal axis. Within the rigid-body modeling framework, a simple way to capture the effect of internal energy dissipation is by using a Kane damper (Kane and Barba, 1966). This mechanism consists of a

fictitious spherical mass contained inside a cavity full of viscous fluid at the spacecraft's center of mass. Assuming that the centers of mass of the spacecraft and the damper remain coincident, a torque proportional to their relative angular velocity will arise:

$$\boldsymbol{\tau}_{\text{damper}} = k_d(\boldsymbol{\omega}_d - \boldsymbol{\omega}) \tag{16}$$

where $\boldsymbol{\omega}$ and $\boldsymbol{\omega}_d$ are the angular velocities of the rigid body and the damper, respectively, with respect to the inertial frame, expressed in the body-fixed frame, and k_d is a damping constant. The damper is treated as a separate rigid body, with its own equations of motion and with only $-\boldsymbol{\tau}_{\text{damper}}$ as an external torque.

3. SLR observations

TOPEX/Poseidon has been a recent focus of the Space Debris Working Group of the ILRS, which has been tracking it since 2014. Observations of the motion of its spin axis and angular velocity have been catalogued and will be discussed here. In order to visualize the spin axis orientation of TOPEX/Poseidon as determined from SLR observations, the Earth-Centered Orbital (ECO) frame will be used. The ECO frame is defined by x_o pointing towards the orbit's ascending node and z_o pointing along the orbit normal. It is therefore rotating with the precessing orbital plane. Fig. 1a shows the ECO frame with respect to the ECI frame (X, Y, Z) as a function of the orbital inclination, i, and right ascension of the ascending node, Ω. The ECO frame is very convenient to visualize the motion of a spacecraft's spin axis: it has long been known that under the sole influence of the gravity-gradient torque, the motion of a spinning satellite's angular momentum vector forms a closed path in this frame (Crenshaw and Fitzpatrick, 1968; Holland and Sperling, 1969). We will use two angles to characterize the orientation of a vector in this frame, as shown in Fig. 1b, θ_{ECO} and λ_{ECO}.

Fig. 2 displays observations of the spin period and spin axis orientation of TOPEX/Poseidon as determined by SLR for the time period from 2014 to 2017 in the ECO frame and taken directly from Kucharski et al. (2017). These observations were obtained by measuring the dis-

tance between the ground laser stations and the retroreflector array during passes over the ground station and analyzing its oscillatory pattern indicating a spacecraft rotation (Kucharski et al., 2017).

From Fig. 2a, one can see that the spin period of the spacecraft is decreasing with time in a nonlinear fashion, frequently experiencing short time periods where an increase occurs (for example, at the beginning and end of 2015), and from Figs. 2b and 2c, we deduce that the spin axis is moving in an evolving oval pattern around a point approximately situated at $\theta_{\text{ECO}} = 98°$ and $\lambda_{\text{ECO}} = -90°$ with a height of $\Delta\theta_{\text{ECO}} = 20°$ and a width of $\Delta\lambda_{\text{ECO}} = 35°$.

Kucharski et al. (2017) also provides insight into the attitude motion of TOPEX/Poseidon by comparing their observations with simulation results. Using a surface geometry model of the satellite, they characterize the influence of radiation pressure and deduce that it is the principal cause of the witnessed decrease of the spin period. However, their study neglects the eddy-current torque and gravity-gradient torques, known to be the cause of the motion of the spin axis, which we will discuss in the next section.

4. Attitude motion and parameter estimation

The D-SPOSE inputs defining the TOPEX/Poseidon scenario will first be outlined in Section 4.1. A novel method to characterize the satellite's moments of inertia using the SLR observations of its rotational motion will then be presented and applied to TOPEX/Poseidon in Section 4.2. Propagation results will be detailed in Section 4.3, where exploratory simulations of the evolution of the rotational variables of TOPEX/Poseidon will be outlined, the goal of which is to provide estimates on the missing spacecraft parameters to characterize the influence of external torques on its rotational dynamics. Section 4.4 will then investigate the influence of specific external perturbations on the determined results, most importantly internal energy dissipation, which will be shown to have a significant influence on the system's characteristics. Finally, predictions of the satellites future attitude state to 2030 will be presented and discussed in Section 4.5.
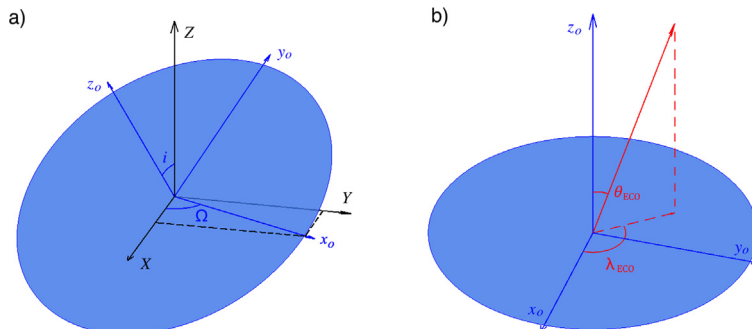

Fig. 1. (a) The Earth-Centered Orbital (ECO) frame as a function of the ECI frame and (b) the definition of the two angles (θ_{ECO} and λ_{ECO}) defining a vector in the ECO frame.
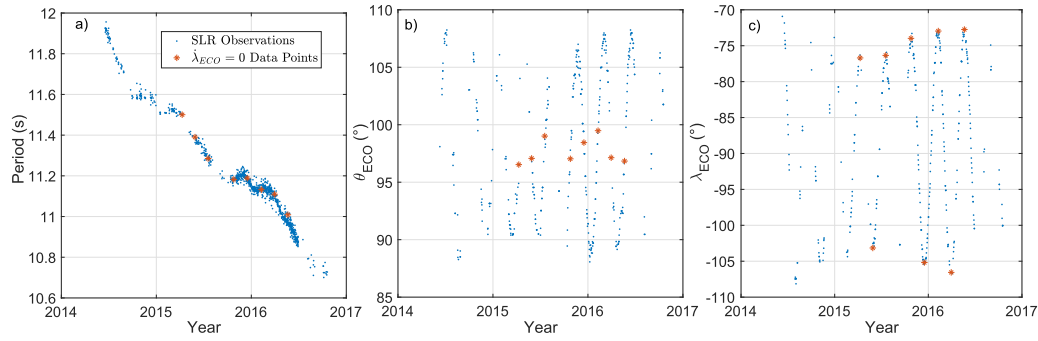
Fig. 2. SLR Observations of TOPEX/Poseidon as a function of time: (a) spin period and (b,c) spin axis orientation in the ECO frame. Points used for the determination of the relationship between the moments of inertia are indicated by red stars.

4.1. Simulation inputs

In order to propagate the attitude motion of the defunct spacecraft, multiple input parameters are needed: information on its initial orbit, attitude, and angular velocity; a precise surface geometry model; information about the satellite's mass and inertia properties; and parameters related to the optical and magnetic properties of the satellite.

The high-repetition rate SLR data obtained for TOPEX/Poseidon for the period 2014–2017 lead to estimates of its spin period and spin axis orientation. The initial orbital elements used for the coupled orbit-attitude propagations were therefore taken from a TLE at the time of the first SLR observations:

```
1 22076U 92052A   14163.17066206 -.00000054  00000-0  28497-4 0  2018

2 22076  66.0407 248.1072 0007707 272.4947 118.5262 12.80986122 21470
```

At approximately that epoch, on June 11, 2014, the spin period of TOPEX/Poseidon was determined to be approximately 11.92 s, with a spin axis defined by $\theta_{ECO} = 98.10°$ and $\lambda_{ECO} = -70.92°$ (Kucharski et al., 2017).

The spacecraft surface geometry model used, made up of 16 triangular surfaces, is shown in Fig. 3 with the solar panel orientation pointing outwards as identified by the red arrow. The spacecraft mass is taken as 2405.4 kg; the center of mass is assumed to be at $\mathbf{c}_p = [0.160 \ -0.418 \ 0.049]^T$ from the center of the box with surface areas $\Delta x \Delta y = 8.32$ m², $\Delta x \Delta z = 8.18$ m², and $\Delta y \Delta z = 4.71$ m²; the solar array measures 3.3 m in width and has a surface area of 25.5 m² (Cerri et al., 2018). All of these parameters, as well as the surface optical coefficients, are taken directly from the International DORIS Service (IDS) macro-model

for TOPEX/Poseidon (Cerri et al., 2018). The mass and center of mass are calculated from pre-launch estimates with the effect from manoeuvres removed (Cerri et al., 2018). Furthermore, the exact orientation of the solar panel is unknown as during the mission it rotated about the axis through the center of the solar panel and satellite body and aligned with the body-frame y-axis; the orientation shown in Fig. 3a is considered to be the 0° case, where rotating it from its current $-z$ orientation towards the x-axis is considered positive in this study. As alluded earlier, there is no available information on the rotational inertial or magnetic properties for TOPEX/Poseidon, nor on the exact orientation of its solar panel. Thus, exploratory simulations with D-SPOSE were employed to help identify the missing inertial properties as well as the orientation of the solar panel.

Simulations were carried out for a period of three years (1096 days) with a time step of 0.5 s, which was determined to be sufficiently small after doing a work-energy balance check and obtaining almost exactly the same results with a time step of 0.1 s. The gravity-gradient torque and gravitational acceleration were calculated using a geopotential up to order and degree 2, as it was previously shown that higher order terms were negligible in the evolution of the attitude motion of large debris (Sagnières and Sharf, 2019). The accelerations and torques due to direct, reflected (albedo), and emitted (infrared) radiation were considered, as well as the eddy-current torque.

As several parameter values of the spacecraft are uncertain, multiple simulations were executed by varying four types of parameters. First, the true moments of inertia
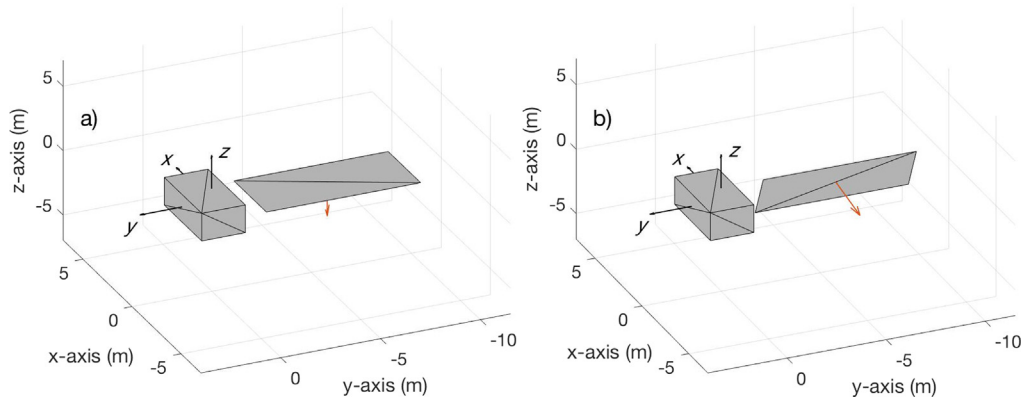
Fig. 3. TOPEX/Poseidon surface geometry model with solar panel orientation at: (a) 0° and (b) 285°.

are unknown. Section 4.2 will showcase a method to derive a relationship between them from observations by assuming that the spacecraft is spinning about its body-frame *z*-axis, as was also determined by observations (Kucharski et al., 2017). Second, although previously estimated to be rotated approximately 285° from the orientation in Fig. 3a, as determined in the study undertaken by the SLR campaign, the exact orientation of the solar panel is unknown (Kucharski et al., 2017). Simulations were therefore performed varying this value from 275° to 295° in 1° increments (the spacecraft geometry with the solar panel orientation at 285° is shown in Fig. 3b). Third, the effect of the eddy-current torque will be investigated and the value of the magnetic tensor, whose principal axes are assumed to be aligned with the principal axes of inertia, $\mathbf{M} = diag\{M_x, M_y, M_z\}$, will be estimated. Finally, the effect of internal energy dissipation will be explored by varying the associated Kane damper parameters. These last three types of parameters will be discussed in more detail in Section 4.4.

4.2. Determining inertia properties

Under the sole effect of the gravity-gradient torque, the spin axis of a rotating body in space will form a closed path in the reference frame fixed with its orbit (Crenshaw and Fitzpatrick, 1968; Holland and Sperling, 1969). Due to this, it is actually possible to obtain a relationship between a spacecraft's moments of inertia from observations of its rotational motion. The following sections will derive a novel method to do so, which could also be applied to other space debris for which we have observations of the motion of their spin axis.

4.2.1. Relationship between spin axis motion and moments of inertia

For a rigid body in a circular orbit, the equation of motion of its angular momentum in the ECO frame, while under the influence of the gravity-gradient torque only, will take the following form (Holland and Sperling, 1969):

$$\frac{d\mathbf{h}}{dt} = \frac{3\mu}{4r^3}\frac{H}{h^2}h_z\begin{bmatrix} -h_y \\ h_x \\ 0 \end{bmatrix} - \boldsymbol{\omega}_o^\times\mathbf{h} \qquad (17)$$

where $\mathbf{h} = [h_x\ h_y\ h_z]^T$ is the angular momentum of the spacecraft in this frame, r is its distance with Earth's center, H is a complex function of the moments of inertia and angular velocity of the spacecraft, to be investigated subsequently, and $\boldsymbol{\omega}_o$ represents the angular velocity of the orbital plane, which is a function of the rate of change of the right ascension of the ascending node, Ω, and the inclination of the orbit, i. For a circular orbit, it is expressed as follows:

$$\boldsymbol{\omega}_o = \begin{bmatrix} 0 \\ \dot{\Omega}\sin i \\ \dot{\Omega}\cos i \end{bmatrix} \qquad (18)$$

Substituting for $\boldsymbol{\omega}_o$ and $\mathbf{h}$ into Eq. (17):

$$\begin{bmatrix} \dot{h}_x \\ \dot{h}_y \\ \dot{h}_z \end{bmatrix} = \frac{3\mu}{4r^3}\frac{H}{h^2}h_z\begin{bmatrix} -h_y \\ h_x \\ 0 \end{bmatrix} - \begin{bmatrix} -h_y\dot{\Omega}\cos i + h_z\dot{\Omega}\sin i \\ h_x\dot{\Omega}\cos i \\ -h_x\dot{\Omega}\sin i \end{bmatrix} \qquad (19)$$

Switching to spherical coordinates using h, θ_{ECO}, and λ_{ECO}, as defined in Fig. 1b (for clarity, the subscript ECO will be dropped in this section):

$$h_x = h\sin\theta\cos\lambda$$
$$h_y = h\sin\theta\sin\lambda$$
$$h_z = h\cos\theta \qquad (20)$$

For a stable principal axis spin, under the sole influence of the gravity-gradient torque, which is conservative, h remains constant and the time derivatives reduce to:

$$\dot{h}_x = h\dot{\theta}\cos\theta\cos\lambda - h\dot{\lambda}\sin\theta\sin\lambda$$
$$\dot{h}_y = h\dot{\theta}\cos\theta\sin\lambda + h\dot{\lambda}\sin\theta\cos\lambda$$
$$\dot{h}_z = -h\dot{\theta}\sin\theta \qquad (21)$$

After the change of variables, Eq. (19) becomes:

$$\begin{bmatrix} \dot{\theta}\cos\theta\cos\lambda - \dot{\lambda}\sin\theta\sin\lambda \\ \dot{\theta}\cos\theta\sin\lambda + \dot{\lambda}\sin\theta\cos\lambda \\ -\dot{\theta}\sin\theta \end{bmatrix} = \frac{3\mu}{4r^3}\frac{H}{h}\cos\theta \begin{bmatrix} -\sin\theta\sin\lambda \\ \sin\theta\cos\lambda \\ 0 \end{bmatrix}$$

$$- \begin{bmatrix} -\dot{\Omega}\sin\theta\sin\lambda\cos i + \dot{\Omega}\cos\theta\sin i \\ \dot{\Omega}\sin\theta\cos\lambda\cos i \\ -\dot{\Omega}\sin\theta\cos\lambda\sin i \end{bmatrix} \tag{22}$$

This is a system of three equations that defines the motion of the spin axis in the ECO frame through the evolution of the angles θ and λ, if all other parameters are known. Alternatively, these equations can be used to identify the value of unknown parameter H/h if observations of the motion of the spin axis are available, which is the case for TOPEX/Poseidon.

For a spacecraft spinning about its principal z-axis (see Fig. 3), as was determined from the SLR campaign (Kucharski et al., 2017), H and h can be written as (Holland and Sperling, 1969):

$$H = I_x + I_y - 2I_z \tag{23}$$
$$h = I_z\omega \tag{24}$$

where ω is the angular velocity of the spacecraft. We can now write our unknown as a function of a non-dimensional parameter I^* which is purely a function of the moments of inertia:

$$I^* = \frac{I_x + I_y - 2I_z}{I_z} \tag{25}$$

so that:

$$\frac{H}{h} = \frac{I^*}{\omega} \tag{26}$$

4.2.2. Estimating the moments of inertia from observations

From the observations presented in Fig. 2, it is possible to determine approximate values for $\theta, \lambda, \dot{\theta}, \dot{\lambda}$, and ω at a specific point in time. Eq. (22) can then be solved for the ratio H/h.

The most simple observations that can be used from Fig. 2 in order to obtain an estimate of I^* occur at times when $\dot{\lambda} = 0$ using the second scalar equation of Eq. (22).

Substituting for $\dot{\theta}$ from the third scalar equation of Eq. (22), $\dot{\lambda} = 0, H/h$ from Eq. (26), and solving for I^*, yields:

$$I^* = \frac{4r^3\omega}{3\mu}\left(-\dot{\Omega}\sin i \csc\theta\sin\lambda + \dot{\Omega}\cos i\sec\theta\right) \tag{27}$$

This equation is valid a long as θ is not a multiple of $\pi/2$.

From the observations of λ_{ECO} in Fig. 2c, it is possible to select 8 points which satisfy the $\dot{\lambda} = 0$ condition. The corresponding values of θ and λ are shown by red stars in Fig. 2b,c and are presented in Table 2 along with the values for r and i, which are obtained from TLEs at the corresponding dates. The value of $\dot{\Omega}$ was also determined from TLEs by assuming it constant over the 2014–2017 period and was found to be $\dot{\Omega} = -2.40433 \times 10^{-5}\,°\,\text{s}^{-1}$. The values for ω are obtained from the corresponding values of the spin period indicated by red stars in Fig. 2a. The derived I^* is presented for each point; the mean and standard deviation calculated from the set of 8 points was found to be $I^* = 0.79 \pm 0.15$, reflecting a significant spread in these estimates. The relationship between the individual moments of inertia therefore becomes:

$$I_x + I_y = (2.79 \pm 0.15)I_z \tag{28}$$

This relationship unequivocally indicates that the spacecraft is rotating about its *minor* principal axis. This will be scrutinized in detail in Section 4.4.3.

4.3. Propagation results

Varying the four types of parameters outlined in Section 4.1, multiple simulations showed good agreement between D-SPOSE propagation results and observations over the time frame 2014–2017. However, the relationship in Eq. (28) was found to not perfectly reproduce observations once the other external perturbations were taken into account. This is due to the fact that the relationship was derived with multiple assumptions, the most important being that the gravity-gradient torque was the only perturbing torque. Nevertheless, after slightly varying the value of I^* and fitting the simulation results to the motion of θ_{ECO} and λ_{ECO}, a more accurate relationship was determined, well within the standard deviation of the original mean:

Table 2
Characteristics of spin axis orientation points where $\dot{\lambda} = 0$.

Date	θ (°)	λ (°)	ω (° s^{-1})	i (°)	r (km)	I^*
10-Apr-2015	96.531	−76.699	31.3030	66.0431	7714.164	0.9417
29-May-2015	97.072	−103.155	31.6061	66.0415	7714.158	0.8537
18-Jul-2015	99.012	−76.348	31.9004	66.0411	7714.153	0.6075
25-Oct-2015	97.036	−73.974	32.1933	66.0402	7714.146	0.8799
16-Dec-2015	98.446	−105.184	32.1751	66.0386	7714.139	0.6779
8-Feb-2016	99.483	−72.958	32.3387	66.0406	7714.136	0.5743
30-Mar-2016	97.133	−106.556	32.4048	66.0420	7714.132	0.87
20-May-2016	96.838	−72.744	32.7008	66.0409	7714.129	0.9311

Table 3
Parameters of the best fit simulations.

Simulation	I_z (kg·m^2)	$M = M_x + M_y$ (S·m^4)	γ (°)
Case 1	70,000	40,000	282
Case 2	60,000	120,000	281
Case 3	50,000	200,000	280
Case 4	40,000	300,000	278

$$I_x + I_y = 2.83 I_z \tag{29}$$

Specific cases where a best fit occurred are presented in Table 3 and the associated simulations are shown in Fig. 4, along with the spin period and spin axis orientation measurements determined from SLR observations in the ECO frame. Simulations where a best fit did not occur will be presented in Section 4.4, where the effects of individual perturbations are studied in more detail.

The results of all of the simulations shown were independent of the individual values chosen for I_x and I_y as long as the relationship in Eq. (29) was upheld. In Table 3, M is defined to be equal to $M_x + M_y$, and, as will be discussed in Section 4.4, the results were found to be independent of the value of M_z.

From the determined values of I_z and M corresponding to good agreements between simulations and observations, an approximate linear relationship between them emerged:

$$I_z = 75,000 - M/8 \tag{30}$$

This relationship was found to hold well for values of $I_z \geqslant 50,000$ kg·m^2, but below that value, the larger difference in the solar panel orientation γ compared to the other cases, as seen in Table 3, breaks the linearity of the identity and the slope of the curve increases slightly. Eqs. (29) and (30) relate the moments of inertia to the magnetic tensor of the spacecraft and represent our best estimates of the dependence between these parameters, as determined by comparing propagation results to observations.

An excellent agreement between the four cases simulation results and the SLR observations can be seen for the evolution of the spin period in Fig. 4. The periods of slower and faster decrease are well captured by the D-SPOSE simulations. The oscillations in the spin axis orientation are also well captured, although small differences in the ampli-

tude of the oscillations between the four cases occur towards the end of the propagation period. Small disagreements in the oscillation amplitudes also appear with respect to SLR observations. This might be due to an external perturbation which is not yet considered in D-SPOSE, possibly the YORP effect, which was previously found to have a significant impact on the attitude of geostationary box-wing satellites (Albuja et al., 2018). Furthermore, although unspecified, uncertainties in the spin axis orientation derived from SLR observations are present and should be kept in mind when assessing the quality of these results.

4.4. Sensitivity study on input parameters

In the previous section, best fit simulation results to observations, while varying parameters that strongly affect the magnitudes of the radiation pressure, induced eddy-currents torques, and gravity-gradient torque, were shown. Simulation results varying specifically the parameters associated with radiation pressure and eddy-currents, as well as internal energy dissipation, are now considered separately in order to highlight the influence of these three torques on the satellite's rotational motion.

4.4.1. Radiation pressure

First, the solar radiation torque is the largest perturbing non-gravitational torque for TOPEX/Poseidon, as was determined by the SLR study. For any spacecraft, the orientation of its solar panel will strongly influence its motion as the pressure resulting from radiation will change both its magnitude and direction. Fig. 5a displays the evolution of the satellite's spin period for five solar panel orientations using the other parameters of Case 2 in Table 3.

One can see that a change in solar panel orientation of only a few degrees from the Case 2 value, keeping all of the other parameters constant, will alter the evolution of the satellite's spin period visibly away from the observations. For the range presented, although the general tendency of the spin period to decrease remains, the actual shape of the spin period evolution varies significantly. The evolution of the spin axis orientation for these simula-
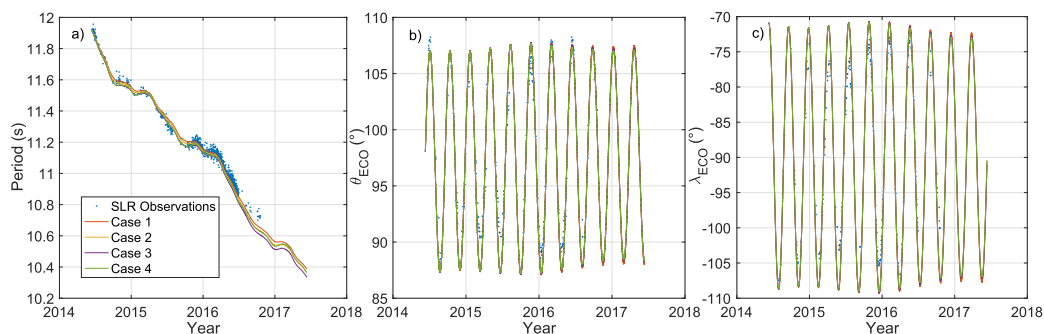

Fig. 4. Evolution of the (a) spin period and (b,c) spin axis orientation of TOPEX/Poseidon from SLR observations and the best fit simulations while varying $I_z, M,$ and γ.
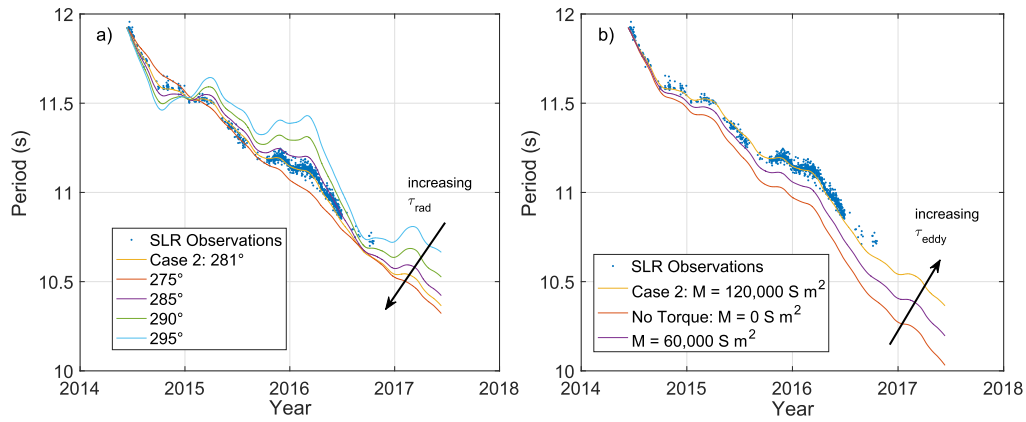
Fig. 5. Evolution of the spin period of TOPEX/Poseidon from SLR observations and simulations for Case 2 while varying the effect of (a) the solar radiation torque due to the orientation of the solar panel and (b) the eddy-current torque due to the spacecraft magnetic properties.

tions, not shown here, are very similar and only differ slightly in the amplitude of the θ_{ECO} and λ_{ECO} oscillations.

4.4.2. Eddy-currents

Second, the eddy-current torque also plays a large role in the satellite's rotational motion. This effect was previously neglected in the SLR observational study. Fig. 5b shows the evolution of the satellite's spin period for different values of the magnetic tensor in the body-fixed frame $\mathbf{M} = diag\{M_x, M_y, M_z\}$. Similarly to the effect of solar radiation, the evolution of the spin axis orientation only showed small changes in the amplitude of its oscillations when varying $\mathbf{M}$ and are not displayed here.

Similarly to the inertia tensor, only partial information can be obtained for this parameter from simulations. The propagation results varying all three components were found to be independent of the value of M_z, and only dependent on the sum of the other two components, $M = M_x + M_y$. This is due to the fact that the spacecraft is spinning about its body-frame z-axis, as can be confirmed analytically from Eq. (5) by substituting for $\boldsymbol{\omega} = [0\ 0\ \omega_z]^T$, $\mathbf{B} = [B_x\ B_y\ B_z]^T$, $\mathbf{M}$ from above, and neglecting the contribution from $\frac{d\mathbf{B}}{dt}$:

$$\boldsymbol{\tau}_{\mathrm{eddy}} = \begin{bmatrix} M_y B_x B_z \omega_z \\ M_x B_x B_z \omega_z \\ -(M_y B_x^2 + M_x B_y^2)\omega_z \end{bmatrix} \qquad (31)$$

As the spacecraft is spinning about its body-frame z-axis quickly compared to its orbital period (approximately 11 s vs. 112 min), not only do the x and y components of the eddy-current torque in Eq. (31) have a negligible influence on the evolution of the satellite's angular motion, but the time-averaged values of the x and y components of the magnetic field in the body-fixed frame will also be equal. Thus, defining $\bar{B}^2$ as the time-average of B_x^2 and B_y^2, an approximate time-average value of the z-component of the eddy-current torque can be written as:

$$\bar{\tau}_{\mathrm{eddy},z} \approx -(M_x + M_y)\bar{B}^2\omega_z \qquad (32)$$

from which it is clear that the only significant parameter is $M = M_x + M_y$.

4.4.3. Internal energy dissipation

The simulations presented previously have so far neglected possible energy dissipation of the spacecraft; this effect must be investigated, especially for a spacecraft which seems to be spinning about its minor principal axis. It is usually expected that energy dissipation eventually transitions a rotating rigid body in space into a major-axis spin; it is in this light that additional simulations were performed with D-SPOSE including the influence of internal energy dissipation, modelled as a Kane damper as presented in Section 2.3.3 (Kane and Barba, 1966). The characteristics of the damper were varied: two moments of inertia were considered, $I_d = 1$ kg·m^2 and $I_d = 10$ kg·m^2; and the damping coefficient k_d was selected to be 1, 0.1, and 0.01 kg·m^2·s^{-1}. These damper characteristics led to an initial perturbing torque on the order of 10^{-7} and 10^{-8} N·m for the respective damper inertias considered, compared to approximately $10^{-2}, 10^{-4}$, and 10^{-5} N·m for the gravity-gradient, radiation, and eddy-current torques, respectively.

Fig. 6 shows the angular velocity and spin axis orientation of TOPEX/Poseidon for the corresponding simulations that were run for a period of three years using the parameters of Case 2 described in Table 3, but with no axisymmetry, randomly choosing $I_x = 94{,}800$ kg·m^2 and $I_y = 75{,}000$ kg·m^2, in order to allow for a clear major principal axis.

As can be seen, for the cases where the effect of internal energy dissipation is expected to be the largest (either due to a small I_d or a large k_d), at some point during the simulation, a transition away from the minor-axis spin and into a major-axis spin occurs. The time taken for the system to transition, however, depends on the damper characteristics. Nevertheless, this phenomenon does not occur for every simulation in the time frame considered, indicating that a minor-axis spin has the potential to endure in stable
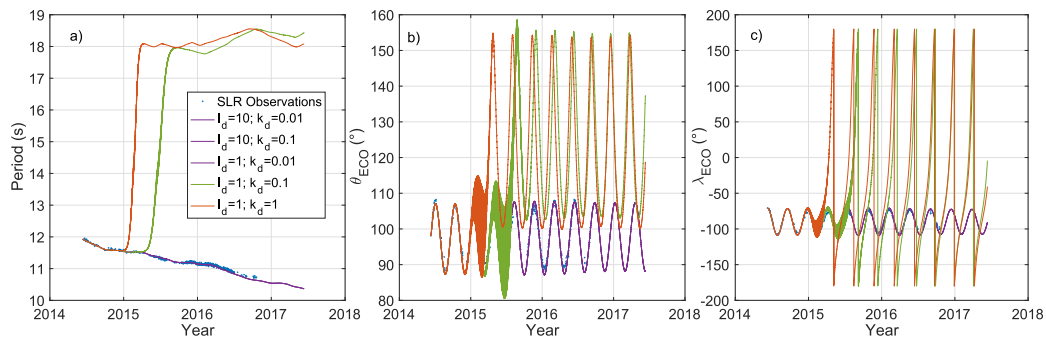
Fig. 6. Evolution of the (a) spin period and (b,c) spin axis orientation of TOPEX/Poseidon from SLR observations and simulations for Case 2 including internal energy dissipation for different values of the damping constant and damper moment of inertia.
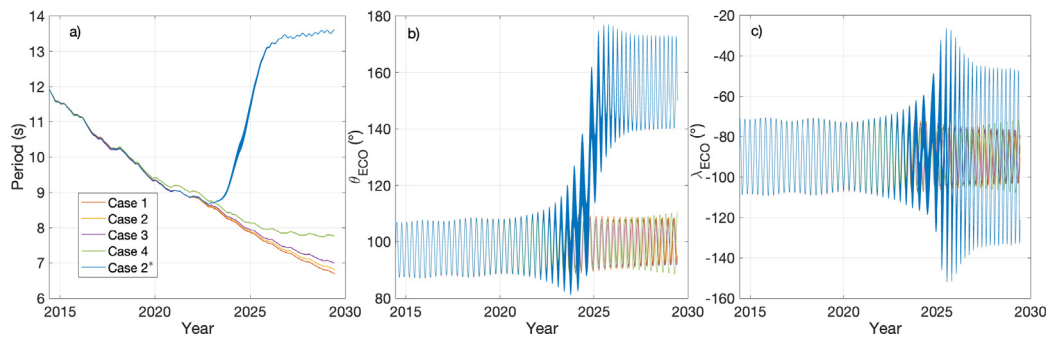

Fig. 7. Predictions of the evolution of TOPEX/Poseidon's (a) spin period and (b,c) spin axis orientation until 2030 from simulations.

manner for quite some time, if internal energy dissipation is small enough.

For the four cases of Table 3, a transition to a major-axis spin within the 2014–2017 time frame occurred only for $I_d = 1$ kg·m^2 and $k_d = 1$ or 0.1. During the simulations, the magnitude of the torque due to the Kane damper systematically increases with time for all of the different scenarios. However, a transition occurred only when the torque exceeded approximately 10^{-4} N·m for the cases presented in green and red in Fig. 6. This allows us to bound the internal damping that exists on the spacecraft.

4.5. Attitude motion predictions to 2030

Simulations for Cases 1 to 4 in Table 3 were performed for a period of 15 years until 2030[2] in order to provide forecasts of the evolution of TOPEX/Poseidon's angular velocity and spin axis orientation and to determine whether the amount of damping within the bounds established in Section 4.4.3 can result in an enduring minor-axis spin. The blue line in Fig. 7 shows the evolution of the spacecraft's spin motion for the entire propagation time frame for the Case 2 simulation without axisymmetry (using the moments of inertia in Section 4.4.3) and and considering a Kane damper with $I_d = 10$ kg·m^2 and $k_d = 0.01$ kg·m^2·s^{-1}

---

[2] This time frame was chosen arbitrarily and is currently the largest time frame available in D-SPOSE due to Sun and Moon ephemerides only being included until then.

(labeled as Case 2*). As can be seen, even in this "small" damping scenario a transition to a major-axis spin eventually occurs around 2023. The time to transition was found to be dependent on the chosen moment of inertia I_z. Since the time to transition was also shown to be dependent on the uncertain damping properties and since the resulting major-axis spin motion will be dependent on the unknown moment of inertia associated with that principal axis (I_x or I_y), no reliable predictions can be put forward for the satellite's future spin motion if a transition ever occurs. The only useful information that can be provided in terms of attitude motion forecasts is if TOPEX/Poseidon stays in a minor-axis spin. As such, Fig. 7 also shows the simulations for Cases 1 to 4 without internal energy dissipation.

From these results, it can be concluded that, if a minor-axis spin is maintained, the satellite's spin period will continue to decrease but with a decreasing rate, dependent on the moments of inertia of the spacecraft. In Case 1, where I_z is the highest, the spin period decreases the fastest. A departure from agreement between the four scenarios starts to occur in the near future, around the year 2020. By 2030, the four simulations show that TOPEX/Poseidon's spin period will have reached approximately 7 s. As was mentioned, if a transition to a major-axis spin does indeed occur, it is impossible at this time to predict when and how the satellite's spin motion will evolve. Initiating a new observation campaign in the near future would shed further light on TOPEX/Poseidon's parameters by comparing to the four cases presented here.
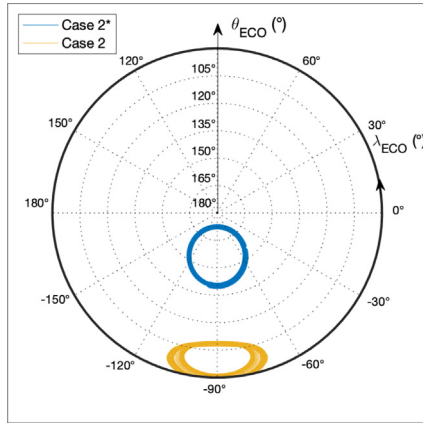
Fig. 8. Evolution of the spin axis orientation of TOPEX/Poseidon using an equidistant azimuthal projection in the ECO frame.

An interesting way to visualize the spin motion of a satellite is by representing its spin axis orientation in an equidistant azimuthal projection of the ECO frame along the line of sight of the orbit normal direction from the negative to the positive z_o-axis. Fig. 8 shows the spin axis orientation in such a projection for the entire Case 2 scenario (in yellow) and the Case 2* scenario after 2027, *i.e.*, after the transition to major-axis spin has occurred (in blue). These results show that the oval pattern of the spin axis orientation mentioned previously persists, but that after the major-axis spin transition, its center evolves along the $-y_o$-axis ($\lambda_{\mathrm{ECO}} = -90°$).

Finally, towards the end of the propagations in Fig. 7a, a decrease of the angular acceleration is seen, suggesting a steady-state value for the angular velocity of the spacecraft will be reached. We hypothesize that this is due to a balance being reached between radiation pressure accelerating the satellite's spin in a constant manner and the eddy-current torque resisting it increasingly due to its proportionality to the spacecraft angular velocity. These opposing effects were annotated in Fig. 5. Considering Eq. (32), one can equate the time-average values of the eddy-current and radiation torques ($\bar{\tau}_{\mathrm{rad}} = -\bar{\tau}_{\mathrm{eddy}}$) to obtain a steady-state value for the angular velocity at which this balance will occur as a function of the spacecraft magnetic properties:

$$\omega_z = \frac{\bar{\tau}_{\mathrm{rad}}}{M\bar{B}^2} \tag{33}$$

Since the time-average of the radiation torque is relatively constant with time, roughly equal to 5×10^{-5} N·m, and the time-average of the square of the x and y components of the magnetic field was determined to be approximately $\bar{B}^2 = 2 \times 10^{-10}$ T^2, both obtained from simulation results, for the value of $M = 300,000$ S·m^4 in Case 4, this balance is predicted to occur at an angular velocity of 0.8 rad·s^{-1}, or equivalently at a spin period of 7.5 s. This is in agreement with the steady-state value approached by Case 4 in Fig. 7a, confirming the hypothesis above.

5. Discussion and summary of findings

In the previous sections, numerical results were presented from a comprehensive study of TOPEX/Poseidon's rotation motion by: (a) investigating its missing parameters through comparisons of observations to simulation results; (b) a detailed assessment of the influence of different perturbations and spacecraft parameters on its rotational motion; and (c) by propagating its rotational motion to a decade into the future. All results in this manuscript were obtained from a novel coupled orbit-attitude propagator developed for such studies, called D-SPOSE. The major findings obtained from this work are as follows:

1. A method to obtain a relationship between the moments of inertia of a spinning space debris from observations of the evolution of the orientation of its spin axis was put forward. Applied to TOPEX/Poseidon, and comparing simulation results to observations, the following relationship providing a good fit was determined, $I_x + I_y = 2.83I_z$, clearly indicating that the spacecraft is rotating about its *minor* principal axis. Moreover, the propagation results over the observation time frame were not affected by the specific values of moment of inertia I_x and I_y, provided the aforementioned relationship was respected.
2. The influence of the gravity-gradient torque, radiation pressure, and eddy-currents on TOPEX/Poseidon was assessed, and it was found that the evolution of the satellite's spin motion was sensitive to each of these effects, with magnitudes of 10^{-2}, 10^{-4}, and 10^{-5} N·m, respectively:
   (a) By varying some of the unknown spacecraft parameters, namely the orientation of the solar panel, the value of I_z, and the magnetic properties, multiple simulations provided a good fit to observations. From these results, a relationship between I_z and the parameter $M = M_x + M_y$ was determined: $I_z = 75,000 - M/8$. This relationship allows us to hypothesize an upper bound for I_z of 75,000 kg·m^2.
   (b) The orientation of the solar panel was determined to be between 278 and 282°, rotating about the negative z-axis from the orientation drawn in Fig. 3a.
   (c) Although the satellite's spin motion was found to be independent of the value of M_z, a range of possible values for M was shown to be 40,000 to 300,000 S·m^4.
3. Analyses of internal energy dissipation using a Kane damper model showed that a transition to a major-axis spin could occur in the near future:
   (a) A lower bound on the Kane damper moment of inertia and an upper bound on the Kane damper coefficient were determined to be 1 kg·m^2 and 0.1, respectively, while the magnitude of the asso-

ciated torque at which such a transition occurred was determined to be 10^{-4} N·m. The current amount of damping, however, is unknown and the time to a transition is therefore impossible to estimate.

(b) If the minor-axis spin endures until 2030, simulations have shown that the spacecraft will be spinning with a period of approximately 7 s at that time. If the motion does evolve into a major principal axis spin, the future motion of the spacecraft cannot be predicted at this time.

Beyond the limitations of the present study, future modeling work and observation campaigns could help provide valuable information on the satellite's rotational motion:

1. While the evolution of the spin period and the oscillations of the spin axis orientation were successfully captured by simulations as presented in this manuscript, a small disagreement in the amplitude of the orientation oscillations was present, possibly due to a missing perturbation, such as the YORP effect.
2. Obtaining a better estimate of the spacecraft's magnetic tensor, using the finite elements method as has been done for Envisat, could help determine the exact value of I_z using the relationship established here (Ortiz Gómez and Walker, 2015).
3. Observational techniques such as inverse synthetic aperture radar (ISAR) imaging could provide additional information on the exact orientation of the solar panel. This would allow for improvement of missing parameter estimates obtained here and would lead to more accurate attitude predictions needed for precise forecasts of the spacecraft attitude and orbit, crucial for space traffic management.
4. Similarly, obtaining a better estimate of the exact orientation of the spin axis in the body-fixed frame, if the principal axis and the z-axis do not coincide, would help provide more accurate simulation results. Work on this is currently on-going by the SLR community (Kucharski et al., 2018).
5. Finally, future observations of TOPEX/Poseidon's spin motion could help distinguish between the four best-fit cases presented. Moreover, if a transition to a major-axis spin is observed, it may be possible to obtain estimates of I_x and I_y.

6. Conclusion

The defunct satellite TOPEX/Poseidon is one of the many objects in the growing population of large space debris orbiting Earth. This spacecraft is of particular interest to the space debris community because of its high probability for conjunction with other functional assets. Studying the rotational dynamics of TOPEX/Poseidon is important: first, for improving our fundamental understanding of rotational motion of space debris and second, for the purpose of improving our prediction capabilities for space situational awareness. However, for this particular satellite, many of its parameters needed to obtain accurate orbital predictions and estimates of its rotational state are currently unknown. This paper presented a comprehensive study of this satellite's rotational motion including estimation of missing inertia parameters, demonstration that the spacecraft is currently in a minor axis spin, and propagation results to 2030. The present work provides new directions for future observational campaigns of TOPEX/Poseidon: these may shed light on several outstanding issues, in particular, if a transition to major axis spin is observed.

References

Albuja, A.A., Scheeres, D.J., Cognion, R.L., Ryan, W., Ryan, E.V., 2018. The YORP effect on the GOES 8 and GOES 10 satellites: a case study. Adv. Space Res. 61 (1), 122–144.

Cerri, L., Couhert, A., Ferrage, P., 2018. DORIS satellites models implemented in POE processing. Tech. Rep. SALP-NT-BORD-OP-16137-CN, International DORIS Service.

Crenshaw, J.W., Fitzpatrick, P.M., 1968. Gravity effects on the rotational motion of a uniaxial artificial satellite. Am. Inst. Aeronaut. Astronaut. J. 6, 2140–2145.

Dormand, J.R., Prince, P.J., 1980. A family of embedded Runge-Kutta formulae. J. Comput. Appl. Math. 6 (1), 19–26.

Earl, M.A., Wade, G.A., 2015. Observations of the spin-period variations of inactive box-wing geosynchronous satellites. J. Spacecraft Rock. 52 (3), 968–977.

Efimov, S., Pritykin, D., Sidorenko, V., 2018. Long-term attitude dynamics of space debris in Sun-synchronous orbits: Cassini cycles and chaotic stabilization. Celest. Mech. Dyn. Astron. 130, 62.

Efimov, S., Pritykin, D., Sidorenko, V., 2018. Defunct satellites in nearly polar orbits: long-term evolution of attitude motion. Open Astron. 27 (1), 264–277.

Fu, L.-L., Christensen, E.J., Jr, C.A.Y., Lefebvre, M., Mnard, Y., Dorrer, M., Escudier, P., 1994. TOPEX/POSEIDON mission overview. J. Geophys. Res.: Oceans 99 (C12), 24369–24381.

Gottlieb, R.G., 1993. Fast Gravity, Gravity Partials, Normalized Gravity, Gravity GradientTorque and Magnetic Field: Derivation, Code and Data. Tech. Rep. 188243, National Aeronautics and Space Administration.

Holland, R.L., Sperling, H.J., 1969. A first-order theory for the rotational motion of a triaxial rigid body orbiting an oblate primary. Astronom. J. 74, 490–496.

Hughes, P.C., 2006. Spacecraft Attitude Dynamics. Dover Publications Inc, Mineola, New York.

IMCCE, 2018. Miriade - the virtual observatory solar system object ephemeris generator. http://vo.imcce.fr/webservices/miriade/. Accessed 2018-08-01.

Kane, T.R., Barba, P.M., 1966. Effects of energy dissipation on a spinning satellite. Am. Inst. Aeronaut. Astronaut. J. 4, 1392–1394.

Kanzler, R., Silha, J., Schildknecht, T., Fritsche, B., Lips, T., Krag, H., 2015. Space debris attitude simulation - ιOTA (In-Orbit Tumbling Analysis). In: Proceedings of the 2015 Advanced Maui Optical and Space Surveillance Technologies Conference. Maui, Hawaii.

Koshkin, N., Korobeynikova, E., Shakun, L., Strakhova, S., Tang, Z.H., 2016. Remote sensing of the EnviSat and Cbers-2B satellites rotation around the centre of mass by photometry. Adv. Space Res. 58 (3), 358–371.

Kucharski, D., Kirchner, G., Bennett, J.C., Jah, M.K., Webb, J.G., 2018. High-definition Photometry – new tool for space debris characterization. In: Proceedings of the 21st International Workshop on Laser Ranging. Canberra, Australia.

Kucharski, D., Kirchner, G., Bennett, J.C., Lachut, M., Sośnica, K., Koshkin, N., Shakun, L., Koidl, F., Steindorfer, M., Wang, P., Fan, C., Han, X., Grunwaldt, L., Wilkinson, M., Rodríguez, J., Bianco, G., Vespe, F., Catalán, M., Salmins, K., del Pino, J.R., Lim, H.-C., Park, E., Moore, C., Lejba, P., Suchodolski, T., 2017. Photon pressure force on space debris TOPEX/Poseidon measured by satellite laser ranging. Earth Space Sci. 4 (10), 661–668.

Kucharski, D., Kirchner, G., Koidl, F., Fan, C., Carman, R., Moore, C., Dmytrotsa, A., Ploner, M., Bianco, G., Medvedskij, M., Makeyev, A., Appleby, G., Suzuki, M., Torre, J.-M., Z., Z., Grunwaldt, L., Feng, Q., 2014. Attitude and Spin Period of Space Debris Envisat Measured by Satellite Laser Ranging. IEEE Trans. Geosci. Remote Sens. 52 (12), 7651–7657.

Kudak, V.I., Epishev, V.P., Perig, V.M., Neybauer, I.F., 2017. Determining the orientation and spin period of TOPEX/Poseidon satellite by a photometric method. Astrophys. Bull. 72 (3), 340–348.

Liou, J.-C., Johnson, N.L., 2006. Risks in space from orbiting debris. Science 311, 340–341.

Montenbruck, O., Gill, E., 2013. Satellite Orbits: Models, Methods, Applications. Springer-Verlag, Berlin Heidelberg.

Ortiz Gómez, N., Walker, S.J.I., 2015. Earth's gravity gradient and eddy currents effects on the rotational dynamics of space debris objects: Envisat case study. Adv. Space Res. 56, 494–508.

Pavlis, N.K., Holmes, S.A., Kenyon, S.C., Factor, J.K., 2012. The development and evaluation of the Earth Gravitational Model 2008 (EGM2008). J. Geophys. Res. 117, B04406.

Sagnières, L.B.M., Sharf, I., 2019. Long-term rotational motion analysis and comparison to observations of the inoperative Envisat. J. Guid. Control Dyn. 42 (2), 364–376.

Sagnières, L.B.M., Sharf, I., Deleflie, F., 2018. Validation of a novel coupled orbit-attitude propagator by comparison to SLR data and light curves. In: Proceedings of the 69th International Astronautical Congress. Abstract ID 46562. Bremen, Germany.

Shan, M., Guo, J., Gill, E., 2016. Review and comparison of active debris capturing and removal methods. Prog. Aerosp. Sci. 80, 18–32.

Stephens, G.L., Campbell, G.G., Vonder Haar, T.H., 1981. Earth Radiation Budgets. J. Geophys. Res. 86, 9739–9760.

Thébault, E., Finlay, C.C., Beggan, C.D., Alken, P., Aubert, J., Barrois, O., Bertrand, F., Bondar, T., Boness, A., Brocco, L., Canet, E., Chambodut, A., Chulliat, A., Coïsson, P., Civet, F., Du, A., Fournier, A., Fratter, I., Gillet, N., Hamilton, B., Hamoudi, M., Hulot, G., Jager, T., Korte, M., Kuang, W., Lalanne, X., Langlais, B., Léger, J.-M., Lesur, V., Lowes, F.J., Macmillan, S., Mandea, M., Manoj, C., Maus, S., Olsen, N., Petrov, V., Ridley, V., Rother, M., Sabaka, T.J., Saturnino, D., Schachtschneider, R., Sirol, O., Tangborn, A., Thomson, A., Tøffner-Clausen, L., Vigneron, P., Wardinski, I., Zvereva, T., 2015. International geomagnetic reference field: the 12th generation. Earth Planets nd Space 67, 79.

Vallado, D., 2013. Fundamentals of Astrodynamics and Applications, fourth ed. Microcosm Press, Hawthorne, California.